S28-34

/02862

TRANSIENT MODELING OF THE THERMOHYDRAULIC BEHAVIOR OF HIGH TEMPERATURE HEAT PIPES FOR SPACE REACTOR APPLICATIONS*

Michael L. Hall and Joseph M. Doster
Nuclear Engineering Department
North Carolina State University

N384177?

ABSTRACT

Many proposed space reactor designs employ heat pipes as a means of conveying heat. Previous researchers have been concerned with steady state operation, but the transient operation is of interest in space reactor applications due to the necessity of remote startup and shutdown. A model is being developed to study the dynamic behavior of high temperature heat pipes during startup, shutdown and normal operation under space environments. Model development and preliminary results for a hypothetical design of the system are presented.

INTRODUCTION

HEAT PIPE DESCRIPTION

A heat pipe is an effective means of transferring heat from one location to another without pumps or moving parts. It consists of a closed system filled with a working fluid. One section of the pipe is placed in a heat source, causing the working fluid to evaporate and the resultant vapor to expand into the remainder of the heat pipe. A different section of the heat pipe is placed in a heat sink, causing the working fluid to condense. The liquid is then conveyed back to the evaporator section by capillary action through a wick structure (see figure 1). The primary heat transfer is due to the latent heat of the working fluid, which results in a nearly isothermal system. The large heat transfer with the accompanying small change in temperature makes the heat pipe equivalent to a structure with a very high thermal conductivity.

DESIGN CONSIDERATIONS FOR SPACE REACTOR USE

Many of the current space based reactor designs for both civilian and military applications employ heat pipes as a means of conveying heat (ref. 1). In these designs, thermal radiation is the principal means for rejecting waste heat from the reactor system, making it desirable to operate at high temperatures.

Lithium is generally the working fluid of choice as it undergoes a liquid-vapor transformation at the preferred operating temperature. There are, however, problems inherent to the choice of a liquid metal as the working fluid. The reactor assembly will have to be launched into orbit, presumably in a cold state with the lithium solid. Therefore, the conditions under which the heat pipe will be self-priming from a frozen state are of great interest. A similar problem is that of restarting the heat pipe after it has been shut down and allowed to solidify; the difference between this problem and the former one being the initial distribution of the solid lithium. An additional concern, particularly in military applications, is the ability of the system to handle extreme bursts of heat input concentrated at a particular location such as might be expected if the satellite were the subject of a military attack.

PURPOSE OF THIS WORK

The steady state behavior of heat pipes has been studied by other researchers (refs. 2,3,4). However, the nature of the previously mentioned processes of remote startup, restart, and reaction to threats necessitates an accurate, detailed transient model of the heat pipe operation. This paper covers the development of a model of the vapor core region of the heat pipe which is part of a larger model of the entire heat pipe thermal response. Other transient heat pipe modeling has been done, including a thermal model of a low temperature heat pipe by Chang and Colwell (ref. 5) which does not include the hydraulic behavior modeled in this paper. Another notable effort involves a modification of the ATHENA code to model an entire space reactor system (ref. 6). This paper differs from the ATHENA code modification in its modeling of diffusion, which the ATHENA code does not treat. In addition, future plans for the model presented in this paper include the modeling of startup from a frozen state.

MODEL DEVELOPMENT

CORE MODEL

The vapor core is modeled using the area averaged Navier-Stokes equations in one dimension, which take into account the effects of mass, energy and momentum transfer. The core model is single phase (gaseous), but contains two components: lithium gas and a noncondensible vapor. The differential form of the equation set used is:

Mixture Continuity Equation

$$\frac{\partial \rho_m}{\partial t} + \frac{\partial}{\partial z}(\rho_m V_m) = \Gamma + \frac{\partial}{\partial z}\left[\rho_m(D_N - D_g)\frac{\partial X_N}{\partial z}\right]$$

Noncondensible Continuity Equation

$$\frac{\partial \rho_N}{\partial t} + \frac{\partial}{\partial z}(\rho_N V_m) = \frac{\partial}{\partial z}\left[[\rho_m D_N]\frac{\partial X_N}{\partial z}\right]$$

Mixture Internal Energy Equation

$$\frac{\partial(\rho u)_m}{\partial t} + \frac{\partial}{\partial z}[(\rho u)_m V_m] = -P_m\frac{\partial V_m}{\partial z} + \Gamma h_g^{pc} - H(\frac{2}{r})(T_m - T_w) + \frac{\partial}{\partial z}\left[\rho_m \{D_N h_N - D_g h_g\}\frac{\partial X_N}{\partial z}\right]$$

Mixture Momentum Equation

$$\frac{\rho_m \partial V_m}{\partial t} + \rho_m V_m\frac{\partial V_m}{\partial z} = -\frac{\partial P_m}{\partial z} - \frac{f_m \rho_m}{2D_h} V_m \left|V_m\right| + \rho_m g$$

State Equation

$$\rho_m = \rho_m (P_m,(\rho u)_m,\rho_N)$$

This equation set presupposes the thermal equilibrium of the lithium gas and the noncondensible, making a second internal energy equation unnecessary. The gases are assumed to have the same convective velocity, eliminating the need for a second momentum equation. However, differing diffusive velocities are allowed with the inclusion of concentration driven mass diffusion (ref. 7). Evaporation and condensation provide mass and energy transfer to and from the liquid wick section. Condensation is assumed to occur only at the liquid-vapor interface, and not by liquid droplet formation in the vapor core. The evaporation rate is given by the following relation:

$$\Gamma = (\frac{2}{r})(\frac{M_g}{2\pi RT_w})^{1/2}[P_{sat}(T_w) - P_g]$$

Convective energy loss to the wick surface is included, but thermal conduction is not included in the model at present. The body forces are assumed zero for a space based system.

This system of coupled nonlinear partial differential equations is solved using a finite difference method. First, the equations are differenced spatially, using a staggered mesh in which the fluid properties are evaluated at the cell centers and velocities are evaluated at cell boundaries. When it is necessary to evaluate a fluid property at a cell boundary, the variable is "donored" (symbolized by a dot over the variable) by setting it equal to the closest "upstream" cell center value, where "upstream" is determined by the velocity at that location. For example, the donored density is defined as:

315

$$\dot{\rho}_{i+1/2} = \begin{cases} \rho_i & \text{if } V_{i+1/2} > 0 \\ \rho_{i+1} & \text{if } V_{i+1/2} < 0 \end{cases}$$

The equations are differenced temporally using a semi-implicit discretization which maintains a linear system in the new time variables while adding increased stability over a fully explicit method. In the semi-implicit method, the velocities in the convective terms and the pressures in the momentum equation are evaluated at the new time step. Finally, the state equation is differenced separately by expanding it about the present time step in a Taylor's series, truncating the series after the linear terms and evaluating the truncated series at the new time step. The final discretized system is:

Mixture Continuity Equation

$$\frac{\rho_{m,i}^{N+1} - \rho_{m,i}^{N}}{\Delta t} + \frac{\dot{\rho}_m^N V_m^{N+1}\big|_{i+\frac{1}{2}} - \dot{\rho}_m^N V_m^{N+1}\big|_{i-\frac{1}{2}}}{\Delta z_i} = \Gamma_i^N + \frac{1}{\Delta z_i}\left[\dot{\rho}_m^N (D_N - D_g)\big|_{i+\frac{1}{2}}\left(\frac{X_{N,i+1}^N - X_{N,i}^N}{\Delta z_{i+\frac{1}{2}}}\right)\right.$$

$$\left. -\dot{\rho}_m^N(D_N - D_g)\big|_{i-\frac{1}{2}}\left(\frac{X_{N,i}^N - X_{N,i-1}^N}{\Delta z_{i-\frac{1}{2}}}\right)\right]$$

Noncondensible Continuity Equation

$$\frac{\rho_{N,i}^{N+1} - \rho_{N,i}^{N}}{\Delta t} + \frac{\dot{\rho}_N V_m^{N+1}\big|_{i+\frac{1}{2}} - \dot{\rho}_m V_m^{N+1}\big|_{i-\frac{1}{2}}}{\Delta z_i} = \frac{1}{\Delta z_i}\left[\dot{\rho}_m^N D_N\big|_{i+\frac{1}{2}}\left(\frac{X_{N,i+1}^N - X_{N,i}^N}{\Delta z_{i+\frac{1}{2}}}\right)\right.$$

$$\left. -\dot{\rho}_m^N D_N\big|_{i-\frac{1}{2}}\left(\frac{X_{N,i}^N - Z_{N,i-1}^N}{\Delta z_{i-\frac{1}{2}}}\right)\right]$$

Mixture Internal Energy Equation

$$\frac{(\rho u)_{m,i}^{N+1} - (\rho u)_{m,i}^{N}}{\Delta t} + \frac{(\dot{\rho} u)_m^N V_m^{N+1}\big|_{i+\frac{1}{2}} - (\dot{\rho} u)_m^N V_m^{N+1}\big|_{i-\frac{1}{2}}}{\Delta z_i} = -P_m^N \frac{(V_{m,i+\frac{1}{2}}^N - V_{m,i-\frac{1}{2}}^N)}{\Delta z_i}$$

$$+\Gamma_i^N h_g^{pc} - H(\frac{2}{r})(T_{m,i}^N - T_{m,i}^N) + \frac{1}{\Delta z_i}\left[\dot{\rho}_m^N(D_N h_N - D_g h_g)\big|_{i+\frac{1}{2}}\left(\frac{X_{N,i+1}^N - X_{N,i}^N}{\Delta z_{i+\frac{1}{2}}}\right)\right.$$

$$\left. -\dot{\rho}_m^N(D_N h_N - D_g h_g)\big|_{i-\frac{1}{2}}\left(\frac{X_{N,i}^N - X_{N,i-1}^N}{\Delta z_{i-\frac{1}{2}}}\right)\right]$$

Mixture Momentum Equation

$$\frac{\dot{\rho}^N_{m,i+\frac{1}{2}}}{\Delta t}(V^{N+1}_{m,i+\frac{1}{2}}-V^N_{m,i+\frac{1}{2}}) + \dot{\rho}^N_{m,i+\frac{1}{2}}(V_m\frac{\partial V_m}{\partial z})\Big|^N_{i+\frac{1}{2}} = -\left(\frac{P^{N+1}_{m,i+1}-P^{N+1}_{m,i}}{\Delta z}\right)_{i+\frac{1}{2}}$$

$$-\left(\frac{f^N_m\dot{\rho}^N_m}{2D_h}V^{N+1}_m\Big|V^N_m\Big|\right)_{i+\frac{1}{2}} + \dot{\rho}^N_{m,i+\frac{1}{2}}g$$

State Equation

$$\rho^{N+1}_{m,i} = \rho^N_{m,i} + (P^{N+1}_{m,i}-P^N_{m,i})\frac{\partial \rho_m}{\partial P_m}\Big|^N_i + \left\{(\rho u)^{N+1}_{m,i} - (\rho u)^N_{m,i}\right\}\frac{\partial \rho_m}{\partial (\rho u)_m}\Big|^N_i$$

$$+ (\rho^{N+1}_{N,i}-\rho^N_{N,i})\frac{\partial \rho_m}{\partial \rho_N}\Big|^N_i$$

These equations, along with a similar momentum equation evaluated at $i-\frac{1}{2}$, constitute a linear algebraic system of six equations in eight variables

$$(\rho^{N+1}_{m,i},\ \rho^{N+1}_{N,i},\ (\rho u)^{N+1}_{m,i},\ V^{N+1}_{m,i+\frac{1}{2}},\ V^{N+1}_{m,i-\frac{1}{2}},\ P^{N+1}_{m,i-1},\ P^{N+1}_{m,i},\ P^{N+1}_{m,i+1})$$

Algebraic manipulation is used to reduce this to a single equation in three variables

$$(P^{N+1}_{m,i+1},\ P^{N+1}_{m,i},\ P^{N+1}_{m,i-1})$$

This single equation is then applied at every node in the physical system to be modeled, resulting in a matrix equation with a tridiagonal structure. The matrix equation is easily solved by a forward-backward sweep (Thomas algorithm) to yield the pressure distribution at the new time step. Back substitution into the discretized equation set then yields the remainder of the variables at the new time step. This method of discretization is similar to the methods used in the TRAC and RELAP computer codes (refs. 8,9).

This finite difference method necessitates limits on the time step size in order to assure stability and accuracy. The Courant limit, which specifies that a fluid element cannot be transferred more than one cell during a time step, is:

$$\Delta t < \min_i \left|\frac{\Delta z_{i+\frac{1}{2}}}{V_{m,i+\frac{1}{2}}}\right|$$

The time step must also satisfy a diffusive Fourier modulus criterion:

$$\frac{1}{2} > \max_i \left|\frac{D_{N,i}\Delta t}{(\Delta z_i)^2}\right| \text{ and } \frac{1}{2} > \max_i \left|\frac{(D_{N,i}-D_{g,i})\Delta t}{(\Delta z_i)^2}\right|$$

The error inherent to truncating the state equation series expansion, referred to as density truncation error, is controlled by decreasing the time step when

the error exceeds a user specified value:

$$\max_{i} \left| \frac{\rho_{m,i}^{N+1} - \rho_m(P_{m,i}^{N+1}, (\rho u)_{m,i}^{N+1}, \rho_{N,1}^{N+1})}{\rho_{m,i}^{N+1}} \right| < E_{max}$$

WALL/WICK MODEL

In the current work, the wall and the wick of the heat pipe are modeled simplistically. A detailed thermohydraulic model of the wick is under development. The primary reasons for including a model of the wall and the wick are: to provide a wall temperature for calculating evaporation rates and convective heat losses for the core model; and to connect the core model with boundary conditions exterior to the heat pipe. Currently, the wall and the wick are modeled as a single entity, using a lumped parameters approach which assumes a constant temperature throughout the wall and the wick at any particular axial node. The mechanisms of heat transfer available to the wall/wick are: exterior heat input, exterior radiative heat loss, convection to the core gas and evaporation at the core-wick interface. The heat balance equation for the wall/wick is then:

$$q''_{in} - \epsilon \sigma T_w^4 + H(T_m - T_w) - (\frac{r}{2})\Gamma h_{fg} = \frac{m_w C_p}{A_s} \frac{dT_w}{dt}$$

After the core model is updated to the new time step, the wall temperature is up-dated by implicitly differencing this equation and solving the resultant nonlinear equation for the wall temperature by a Newton-Raphson rootfinding technique at every axial location. Exterior boundary conditions vary along the length of the heat pipe. In the evaporator section, a total net heat flux into the heat pipe is specified. In the adiabatic section of the heat pipe, all heat loss mechanisms are set to zero. Radiation is the only means of heat loss assumed in the condensing end of the heat pipe.

RESULTS

MODEL CONDITIONS

The model has been applied to a 2.0m heat pipe that consists of an evaporator section of $z\epsilon[0,.3]$, an adiabatic section for $z\epsilon[.3,1.5]$, and a condenser section for $z\epsilon[1.5,2]$. These sections are used only to determine which boundary conditions to apply: heat input, zero heat flux, or heat output. A starting temperature of 700K is used. The heat pipe is operated at 15kW throughput for 20s in order to heat it up and then the power is dropped to the desired operating condition of 1.184kW. A heat pipe of this design would normally operate at 15kW and 1500K, but the highest throughput the model will allow with an operating temperature of 1500K is 1.184kW if the only means of heat loss is radiative cooling. Initially, the heat pipe is filled with a noncondensible gas (air) at a pressure of 250Pa.

ANALYTICAL STEADY STATE RESULTS

Most of the steady state heat pipe analysis has been based on Cotter's early work (ref.3). These analyses have been primarily concerned with pointing out limits to the heat transfer capability of the heat pipe in the form of sonic, boiling, wicking, and entrainment limits. Of greater importance to this work is the application of Cotter's theory to predict pressure, temperature, and velocity distributions inside the heat pipe's vapor core. Cotter's theory assumes that the temperature distribution is simply a constant value. The velocity distribution, assuming constant heat addition in the evaporator and constant heat rejection in the condenser, linearly increases from zero to Q_t/h_{fg} in the evaporator, remains constant through the adiabatic section, and then linearly decreases to zero again in the condenser. The predicted steady state pressure distribution is more complicated and is presented in Figure 2, as calculated by the HTPIPE code (ref. 4).

EXPERIMENTAL STARTUP OBSERVATIONS

In his later work, Cotter describes three basic modes of heat pipe startup that have been observed experimentally (ref. 10). The first mode, a uniform startup, occurs when the vapor density is high, and there is continuum flow throughout the heat pipe. A second, frontal startup mode is observed when the vapor density is so low that free molecular flow effects are important. This mode has a continuum to free molecular flow transition region that moves down the length of the heat pipe and causes the progressing, frontal temperature distribution. The third startup mode is also frontal, caused now by the presence of a noncondensible gas. This gas is swept out of the evaporator section and forms a plug that is compressed into the condenser end. The interface between the two gases is sharply defined and the temperature change across this front is more abrupt than that of the second startup mode.

MODEL RESULTS

The heat pipe was modeled for a period of greater than six minutes model time. The work was done in FORTRAN on a VAX-11/750 and required approximately 36 hours of CPU time. Results from the first 20 seconds (startup results) and from the state of the model at 360 seconds (when many of the primary fluctuations have died out and the model is approaching steady state) are presented.

Wall temperature increases evenly across the evaporator section during startup, with the rest of the heat pipe following behind (Figure 3). The step changes in temperature at the end of the evaporator are due to the simplistic wall/wick model where axial heat transfer has been neglected. The adiabatic and condenser wall sections are heated by condensation and convection from the central gas core. The mixture temperature generally follows the wall temperature (Figure 4). However, the sharp temperature changes present in the wall are not present in the core because of the convective transport of the hot gas. The frontal startup shown in the model resembles a combination of the second and third startup modes observed by Cotter, which should be expected due to the presence of the

noncondensible and the low vapor densities. At 16 seconds, both the mixture and wall temperatures have assumed flat profiles.

The lithium gas pressure increases with time as the wall temperature increases and condensation is inhibited (Figure 5). The lithium gas produced in the evaporator section travels down the heat pipe, pushing the noncondensible gas ahead of it (Figure 6). By 16 seconds, the noncondensible has been packed into the end of the condenser with the lithium occupying the remainder of the heat pipe. The moving noncondensible-lithium interface is sharply defined, as observed by Cotter. The total pressure remains relatively flat throughout the startup transient.

The mixture velocity exhibits a maximum during the startup of the heat pipe (Figure 7), with the distribution peaking at the end of the evaporator section. The magnitude of the peak increases quickly to its maximum value at 4 seconds, and then decreases slowly as lithium gas is transported further down the heat pipe before condensing. The maximum value of 700 m/s is much larger than steady state values of around 10 m/s.

The evaporation rate during startup increases rapidly to a rather constant value in the evaporator section (Figure 8). Note that the 1-second line is approximately at zero: an evaporation rate above that line indicates net evaporation, while an evaporation rate below that line indicates condensation. Due to the relatively cold wall temperature beyond the evaporator section, the lithium gas begins condensing as soon as it leaves the evaporator, with the effective condensing length of the heat pipe increasing with time. Condensation increases when the gas reaches the condenser section, which is radiatively cooled.

After 360 seconds of model time both the wall and the mixture temperature show a drop of less than 20 degrees from the evaporator to the condenser (Figures 9,10), not including the plug of noncondensible gas in the condenser end. The temperature variations in this plug of gas are due to relatively poor low velocity heat transport of the noncondensible as compared to condensation, and the lack of conduction in the core model which would reduce the 40 degree temperature gradient. The pressure distributions show that the noncondensible has been compacted into the condenser end (Figure 11). Mixture pressure is very flat, but does have some variation which has been magnified greatly in Figure 12. This distribution has the same general shape as the steady state distribution calculated from the HTPIPE code (Figure 2).

The mixture velocity distribution at 360 seconds consists of three linear sections (Figure 13). The evaporator section is linearly increasing, which coincides with Cotter's theory on steady state heat pipe behavior. The condenser section is linearly decreasing in velocity, which also agrees with Cotter's theory. However, the velocity profile in the adiabatic section is not flat, as Cotter's theory predicts, but rather decreases linearly with a different slope from the condenser region. The reason for this behavior can be seen in the evaporation rate (Figure 14). The evaporation rate is constant in both the evaporator and condenser section, as Cotter assumes, but has a nonzero value in the adiabatic section. The nearly constant condensation rate in the adiabatic section causes the velocity in that section to resemble the linearly decreasing velocity of the condenser. Condensation in the adiabatic section indicates that the system has not fully achieved a steady state condition.

Diffusion was taken out of the model in order to determine its effect on heat

pipe performance. Figures 15 through 20 (in which diffusion has been neglected) correspond to Figures 3 through 8. There is little difference between the sets of plots, indicating that diffusion does not affect the heat pipe performance during this transient.

SUMMARY

A transient model of the vapor core of high temperature heat pipes has been developed. Model trends show good agreement with both analytical steady state calculations and experimentally observed startup behavior. Diffusion does not have a large effect on heat pipe performance for this particular transient. Investigation into the transient conditions during which diffusion has a more prominent effect is planned. Future modeling efforts will include a thermohydraulic model of the wick region with provisions for startup from a solid state and conduction in the vapor core.

SYMBOLS

A_s — surface area of the liquid—vapor interface (m^2)

c_p — specific heat (J/kg·K)

D — mass diffusion coefficient (m^2/s)

D_h — hydraulic diameter (m)

E_{max} — maximum tolerable error

f — friction factor

g — acceleration due to gravity (m/s^2)

H — heat transfer coefficient (J/m^2·K)

h — enthalpy (J/kg)

h_{fg} — latent heat of evaporation (J/kg)

h_g^{pc} — enthalpy of the lithium gas upon changing phase (J/kg)

M — molecular weight (kg/kg·mole)

m — mass (kg)

P — pressure (Pa)

Q_t — total heat throughput (W)

q_{in}'' — heat flux incident on the heat pipe (W/m^2)

R — gas constant (J/kg·mole·K)

r — inner wick radius (m)

T — temperature (K)

t — time (s)

u — internal energy (J/kg)

V — velocity (m/s)

X — mass fraction

z — axial distance (m)

Greek Letters:

Γ — evaporation rate (kg/m^3·s)

Δ — difference between two values, e.g. $\Delta X_i = X_{i+1/2} - X_{i-1/2}$, $\Delta X_{i+1/2} = X_{i+1} - X_i$

ε — emissivity

ρ — density (kg/m^3)

σ – Stefan–Boltzmann constant $(J/m^2 \cdot s \cdot K^4)$

Subscripts:

g   – lithium gas
i   – spatial node
m   – mixture
N   – noncondensible gas
sat – vapor–wick saturation value
w   – wick/wall

Superscript:

N   – time step

REFERENCES

1. Jay E. Boudreau and David Buden, "A New Generation of Reactors for Space Power," Symposium on Advanced Reactor Systems, Washington, DC, 1982.

2. P. D. Dunn and D. A. Reay, Heat Pipes (Pergamon Press, Ltd., Oxford, NY, 1976).

3. T. P. Cotter, "Theory of Heat Pipes," LA–3246–MS, 1965.

4. F. C. Prenger, Jr., "Heat Pipe Computer Program (HTPIPE) User's Manual," LA–8101–M, 1979.

5. W. S. Chang and Gene T. Colwell, "Mathematical Modeling of the Transient Operating Characteristics of a Low–Tempeature Heat Pipe," submitted to Numerical Heat Transfer.

6. C. D. Fletcher and H. Chow, "Simulation of the General Electric SP–100 Space Reactor Concept Using the ATHENA Computer Code," submitted to the Third Symposium on Space Nuclear Power Systems, January 1986.

7. R. B. Bird, W. E. Stewart, and E. N. Lightfoot, Transport Phenomena (John Wiley and Sons, Inc., New York, 1960).

8. "TRAC–P1A/MOD1––An Advanced Best–Estimate Computer Program for Pressurized Water Reactor Loss–of–Coolant Accident Analysis," Los Alamos National Laboratory report.

9. V. H. Ransom, et al., RELAP5/MOD2 Code Manual, Volume 1: Code Structure, System Models and Solution Methods, EGG–SAAM–6377, April 1984.

10. T. P. Cotter, "Heat Pipe Startup Dynamics," Thermionic Conversion Specialist Conference, Palo Alto, CA, 1967.
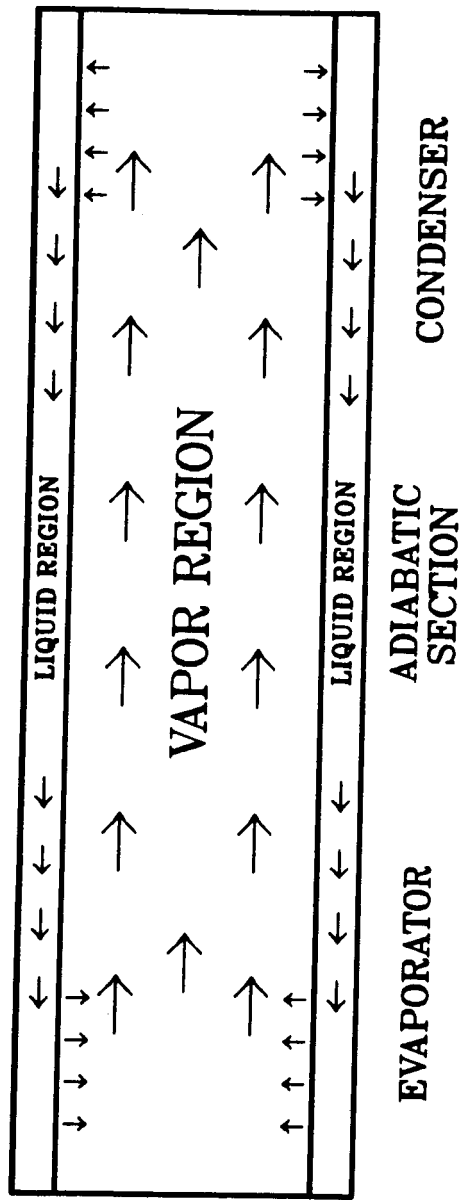
Figure 1. Heat pipe schematic diagram
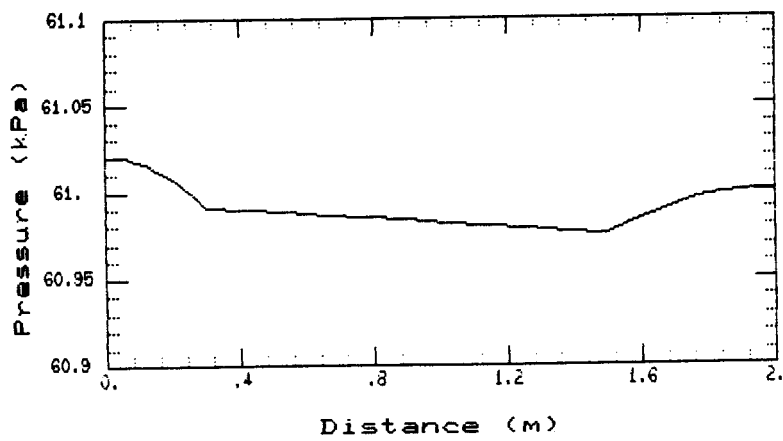
Figure 2. Steady state pressure profile (HTPIPE)
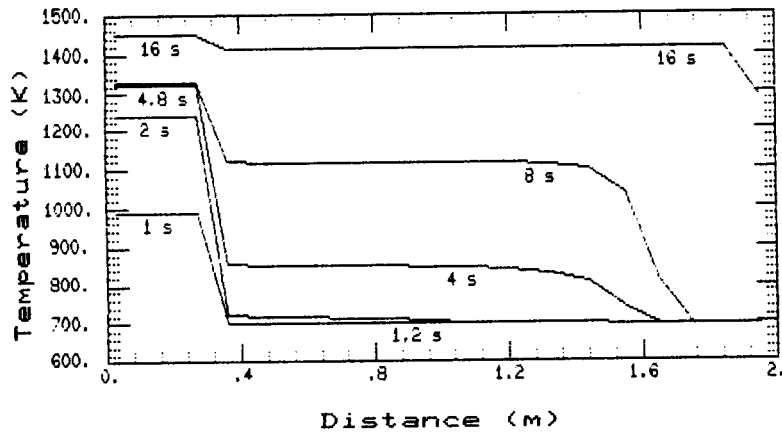
Figure 3. Wall temperature (startup)
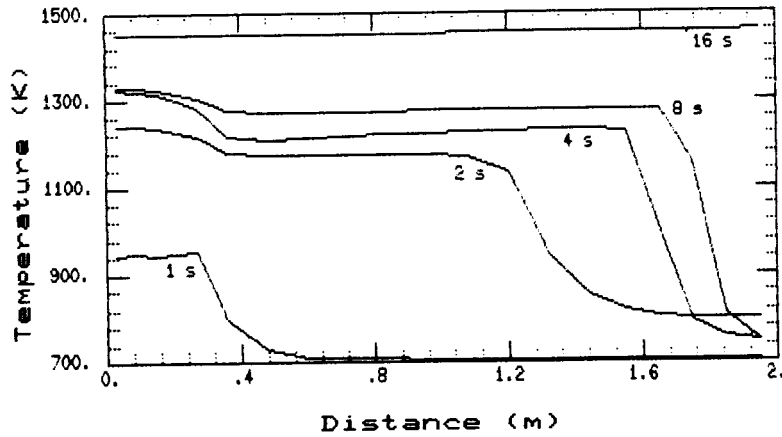
Figure 4. Mixture temperature (startup)
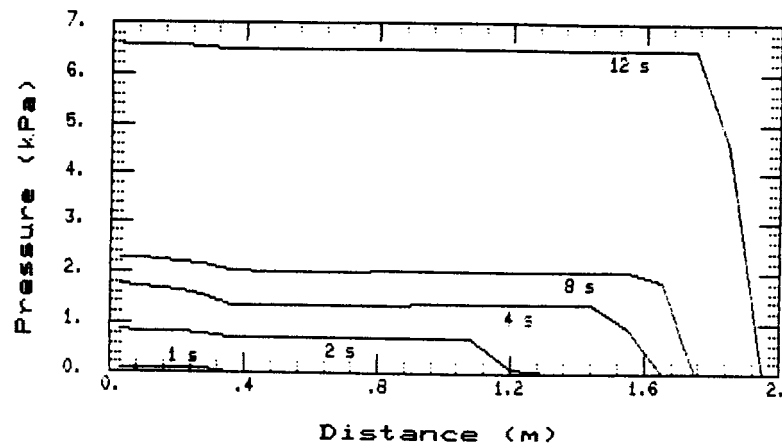
Figure 5. Lithium gas pressure (startup)
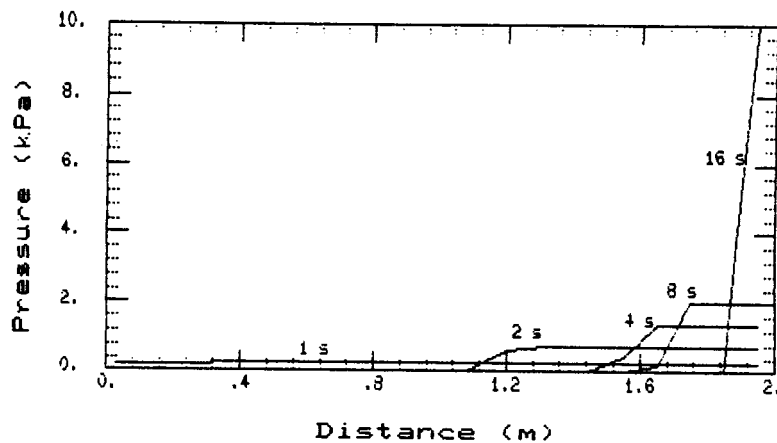
Figure 6. Noncondensible pressure (startup)
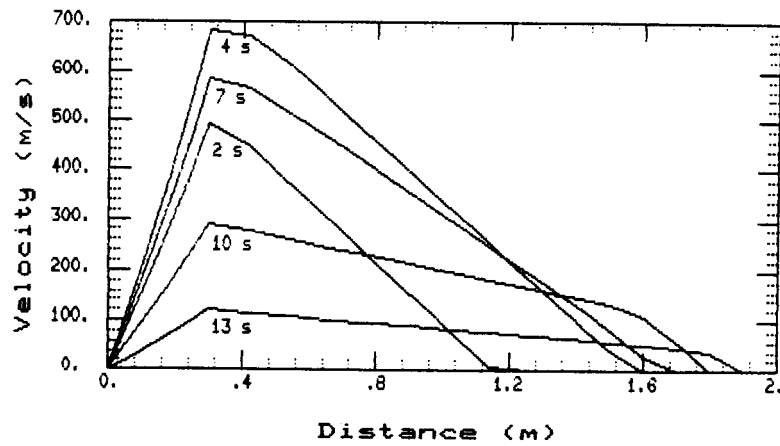

Figure 7. Mixture velocity (startup)
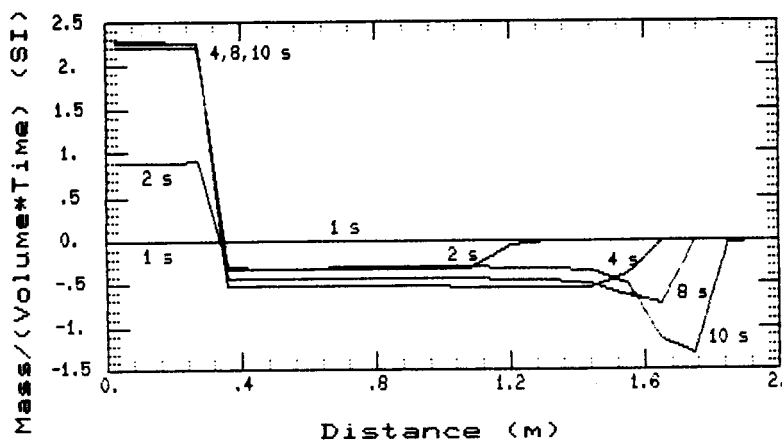
Figure 8. Evaporation rate (startup)
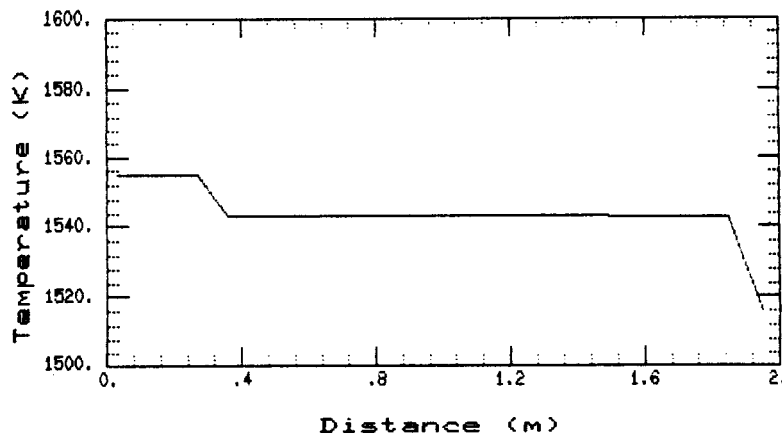

Figure 9. Wall temperature (360 seconds)
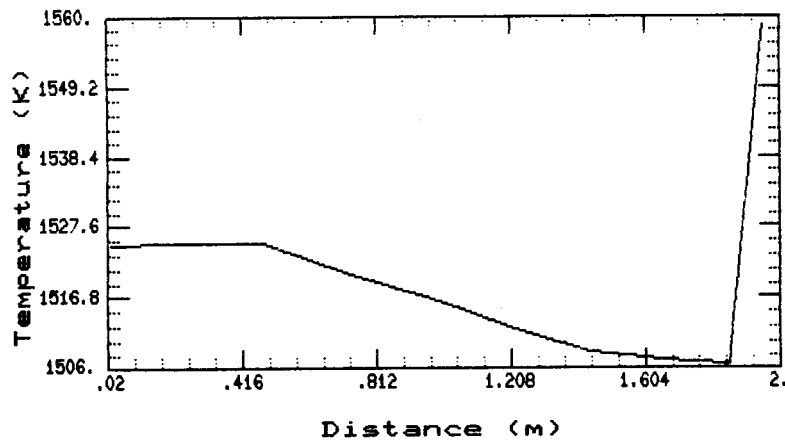

Figure 10. Mixture temperature (360 seconds)

326
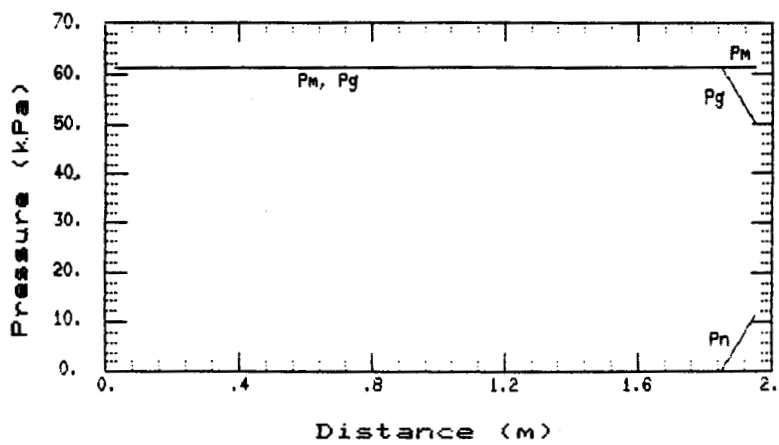
Figure 11. Pressures (360 seconds)
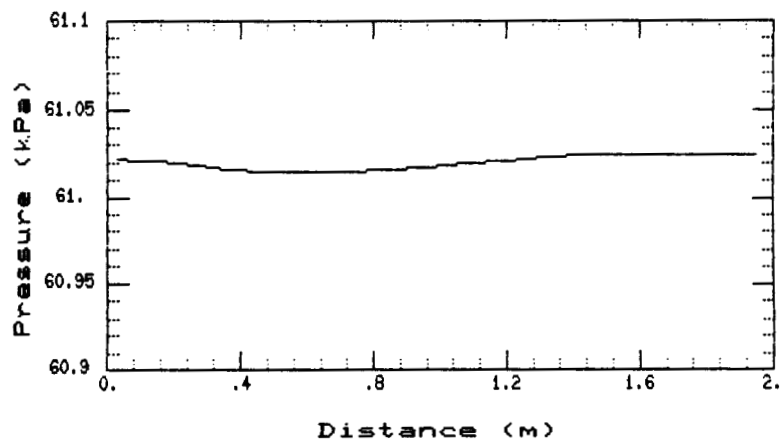
Figure 12. Mixture pressure (360 seconds)
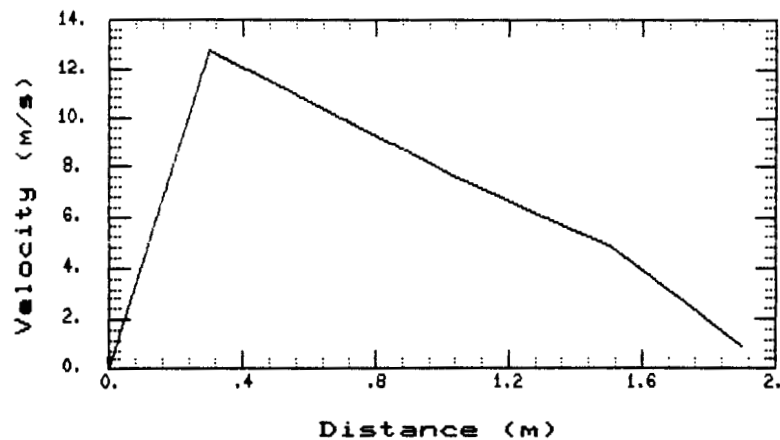
Figure 13. Mixture velocity (360 seconds)

327
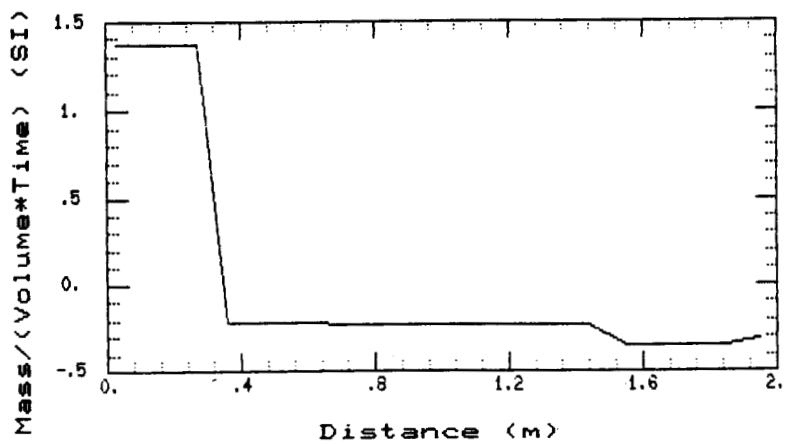
Figure 14. Evaporation rate (360 seconds)
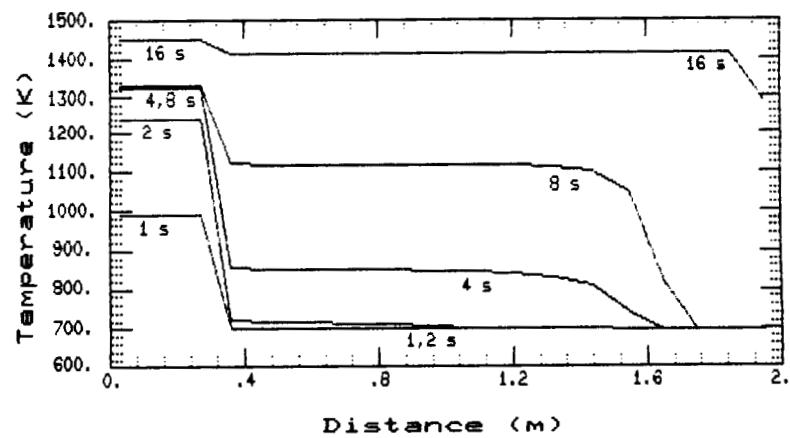
Figure 15. Wall temperature (startup, no diff)
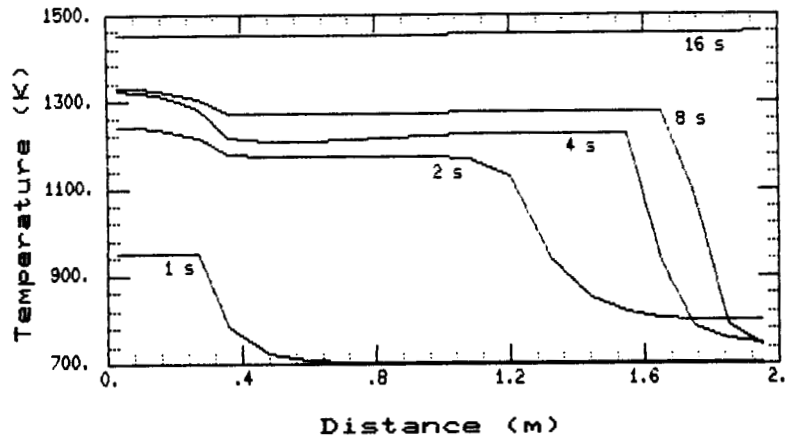
Figure 16. Mixture temperature (startup, no diff)
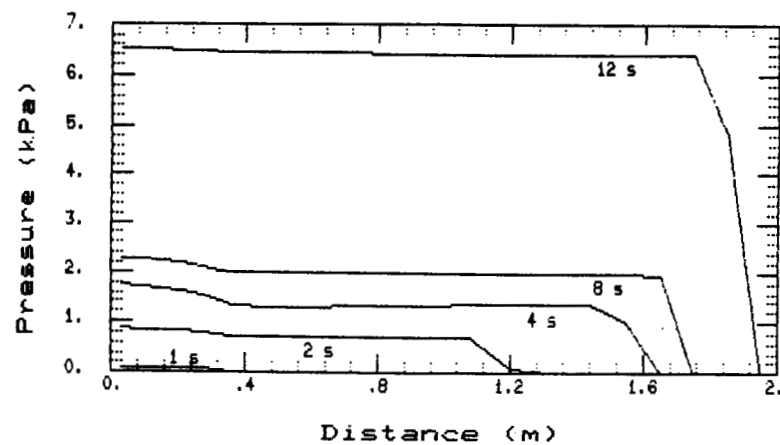
Figure 17. Lithium gas press. (startup, no diff)
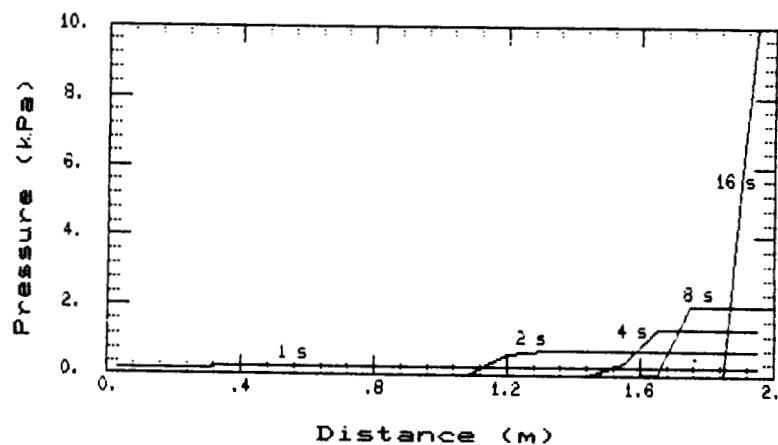

Figure 18. Noncondensible press. (startup, no diff)
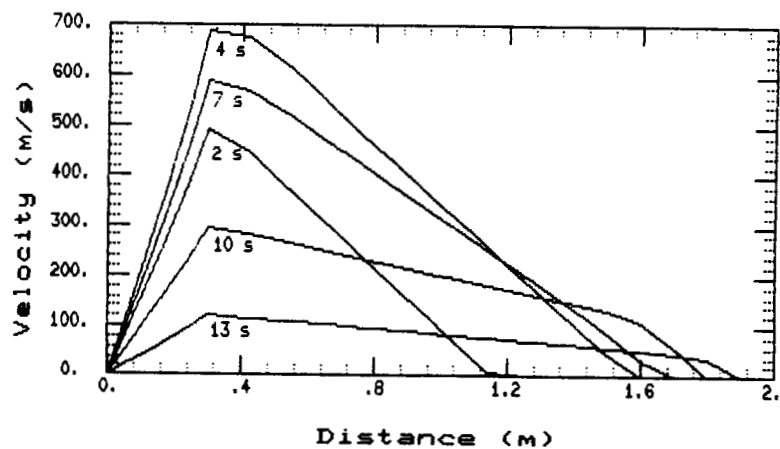

Figure 19. Mixture velocity (startup, no diff)

329
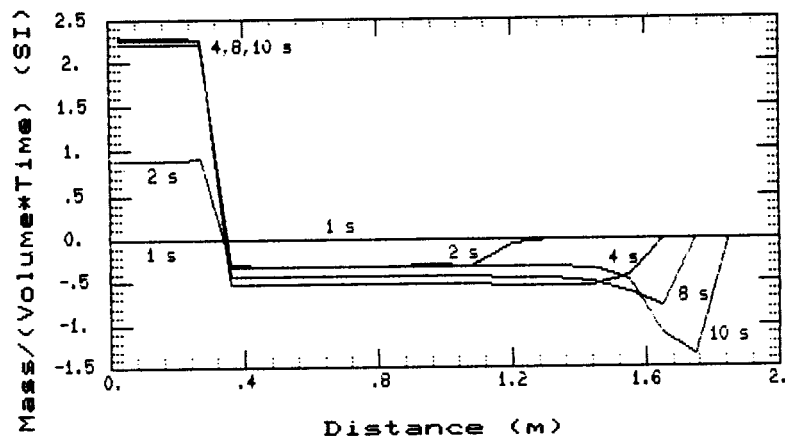
Figure 20. Evaporation rate (startup, no diff)